Review

Visualization of chemical reaction dynamics:
Toward understanding complex polyatomic reactions

By Toshinori Suzuki[*1,*2,†]

(Communicated by Hiroo Inokuchi, m.j.a.)

Abstract: Polyatomic molecules have several electronic states that have similar energies. Consequently, their chemical dynamics often involve nonadiabatic transitions between multiple potential energy surfaces. Elucidating the complex reactions of polyatomic molecules is one of the most important tasks of theoretical and experimental studies of chemical dynamics. This paper describes our recent experimental studies of the multidimensional multisurface dynamics of polyatomic molecules based on two-dimensional ion/electron imaging. It also discusses ultrafast photoelectron spectroscopy of liquids for elucidating nonadiabatic electronic dynamics in aqueous solutions.

Keywords: molecular beam, chemical reaction, nonadiabatic transition, imaging, scattering, photoelectron spectroscopy

1. Introduction: imaging reactive molecular scattering

Liquid is the most important phase of matter in chemistry and biology. However, it is very difficult to study bimolecular reaction dynamics in liquids due to the billions of collisions occurring per second in liquids. These collisions obscure the initial conditions of the reacting pair and obliterate the nascent product state distributions. Consequently, the most detailed studies of bimolecular reactions employ crossed atomic and molecular beams in vacuum. The crossed-beam technique prepares well-defined quantum states and velocities of reactants and interrogates the products and their velocities. This method was first demonstrated in 1955.[1)] It was initially applied only to the reactions of alkali metal atoms due to its low detection sensitivity of products; this period of research is often referred to as the "alkali age" of molecular beam research. In the late 1960s, a universal detector was developed. This detector employed electron bombardment ionization

and quadrupole mass analysis,[2)] and it enabled the velocity distribution (*i.e.*, speed and angular distributions) of virtually any chemical species to be measured with mass selection. Crossed-beam experiments using this universal detector revealed fundamental aspects of chemical reaction dynamics for which the Nobel Prize for Chemistry was awarded to Lee and Herschbach (with Polanyi) in 1986. However, the universal detector is unable to select the quantum (rotational, vibrational and electronic) states of reaction products, which limits the usefulness of this methodology. Since the 1970s, efforts have been made to develop new experimental techniques to perform quantum-state-selective measurements of the velocity distributions of reaction products.[3)–8)] Of these techniques, two-dimensional ion imaging is the most powerful.[9),10)]

Experimental and theoretical studies since the 1950s have greatly advanced our understanding of atom + diatom reactions such as $H + H_2$ and $F + H_2$.[11)–18)] Extension of such studies to atom + polyatom and diatom + diatom systems is critical for elucidating the multidimensional dynamics of polyatomic molecules. When studying these reactions, it is essential to measure the velocity distributions of quantum-state-selected reaction products. To understand why, we compare the atom + diatom reaction, $O(^1D_2) + H_2 \rightarrow OH + H$ and the atom + polyatom

[*1] Department of Chemistry, Graduate School of Science, Kyoto University, Kyoto, Japan.
[*2] RIKEN, Saitama, Japan.
[†] Correspondence should be addressed: T. Suzuki, Department of Chemistry, Graduate School of Science, Kyoto University, Kyoto 606-8502, Japan (e-mail: suzuki@kuchem.kyoto-u.ac.jp).
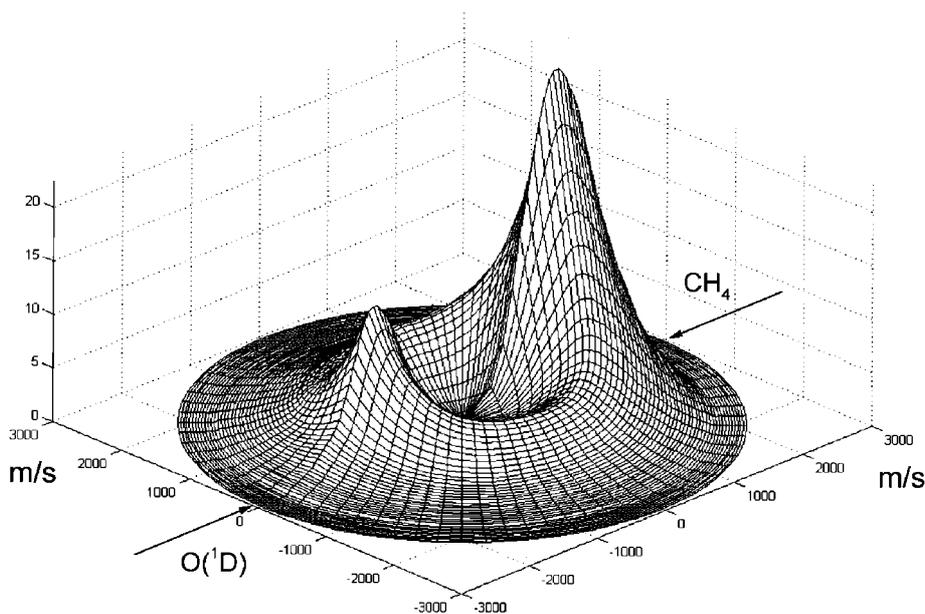
Fig. 1. Center-of-mass speed and angular distribution of OH produced by $O(^1D) + CH_4$ reaction at a collision energy of 6.5 kcal/mol. The distribution was determined by simulation of the experimental data obtained by the universal crossed-beam apparatus. Reproduced with permission from Ref. 23.

reaction, $O(^1D_2) + CH_4 \rightarrow OH + CH_3$. If the $O(^1D_2)$ and H_2 beams collide with a well-defined kinetic energy, the velocity distribution of H can be used to determine the internal energy distribution of OH by applying the energy and momentum conservation laws.[19)–22)] However, for the reaction $O(^1D_2) + CH_4$, *mass*-selected velocity measurements of OH or CH_3 do not provide the internal energies of the products OH or CH_3 because their velocities are determined by the total internal energies of both OH and CH_3.

Figure 1 presents the velocity distribution of the OH product of the reaction $O(^1D_2) + CH_4 \rightarrow OH + CH_3$ measured using the universal detector.[23)] The anisotropic angular distribution indicates that the reaction does not generate any long-lived reaction intermediate. On the other hand, this structureless speed distribution is not very useful for elucidating the dynamics. The following explanation describes how quantum-state-selected measurements of products provide deeper insights into the dynamics of the reaction $O(^1D_2) + CH_4$.

The $O(^1D_2)$ state is a highly reactive metastable state of an O atom. Since $O(^1D_2)$ is the primary photodissociation product of stratospheric ozone, $O_3 + h\nu \rightarrow O(^1D_2) + O_2(^1\Delta_g)$, the $O(^1D_2)$ reaction is of great interest for atmospheric chemistry. $O(^1D_2)$ reactions with an aliphatic hydrocarbon are representative "insertion" reactions as they proceed via a complex produced by inserting $O(^1D_2)$ into a chemical bond. The high reactivity of $O(^1D_2)$ originates from the attractive long-range force in the insertion pathway: in the case of $O(^1D_2) + CH_4$, $O(^1D_2)$ can attack the C–H bond of methane to form a methanol intermediate that subsequently breaks up into $CH_3 + OH$ (the insertion pathway). On the other hand, product analyses performed in the 1960s and 1970s suggest the existence of a direct "abstraction" pathway:[24),25)] $O(^1D_2)$ attacks the H atom collinearly with the C–H bond and abstracts the H atom to form $CH_3 + OH$ without any reaction intermediate (the abstraction pathway). The abstraction pathway has an activation barrier. The origins of these two pathways can be understood by considering the reaction $O(^1D_2) + H_2(^1\Sigma_g^+) \rightarrow OH(^2\Pi) + H(^2S)$. The electronic symmetry of this system is either $^1A'$ or $^1A''$ depending on the reflection symmetry of the electronic wave function of $O(^1D_2)$ relative to the molecular plane defined by the three atoms because the electronic wave function of $H_2(^1\Sigma_g^+)$ is symmetric for reflection. Since $O(^1D_2)$ is a five-fold degenerate state, five potential energy surfaces are created by interaction with H_2. Of these, the $1^1A'$ state is correlated with the ground electronic state of H_2O and provides the insertion pathway, while the $1^1A''$ state leads to the abstraction pathway. A similar symmetry argument applies to the local symmetry

of the O, C and H atoms in $O(^1D_2) + CH_4(^1A_1) \rightarrow OH(^2\Pi) + CH_3(^2A_2'')$ and it explains the duality of the reaction pathway.

In the early 1990s, we used infrared diode laser absorption spectroscopy to measure the vibrational state distribution of CH_3 radicals in the reaction $O(^1D_2) + CH_4 \rightarrow OH + CH_3$.[26] Radicals were observed in low vibrational states of the ν_2 (out-of-plane bending) mode, even though the structure of the CH_3 moiety changes from pyramidal to planar during the reaction.[26] This result contrasts with the inverted vibrational distribution of OH.[27] These studies of the rovibrational state distributions of the products could not identify the elusive abstraction pathway.[26),27]

The scattering distributions (especially the backward scattering distribution) of the products are critical for identifying the abstraction pathway. Since the insertion pathway has long-range attractive interactions between $O(^1D_2)$ and CH_4 in the entrance channel, collisions with large impact parameters (*i.e.*, glancing collisions) should dominate the reaction. Consequently, the CH_3 products of the insertion pathway are strongly scattered in the forward direction (*i.e.*, the initial beam direction of CH_4). If the CH_3OH complex has a sufficiently long lifetime, it will rotate before breaking up into CH_3 and OH, so that the angular distribution of OH will extend in the backward direction.[28] On the other hand, the abstraction pathway has an extremely short reaction time so that the product angular distribution is predominantly determined by the transition state geometry. The transition state has a nearly collinear O–H–C geometry, which provides backward scattering. The angular distribution in Fig. 1 exhibits strong forward scattering, indicating that insertion is the main pathway and that the methanol complex has a very short lifetime. The distribution reveals the backward scattering component, but it is not clear whether the back-scattered products originate from the "osculating" (short-lived) CH_3OH complex[28] in the insertion pathway or from an abstraction pathway.

In order to investigate $O(^1D_2)$ reaction with methane in greater detail, we constructed a crossed molecular beam apparatus with two-dimensional ion imaging, as schematically shown in Fig. 2.[29)–32] The key component of this apparatus is the intense $O(^1D_2)$ beam source that employs 157 nm photodissociation of O_2 [$O_2 + h\nu \rightarrow O(^1D_2) + O(^3P_J)$]. O_2 is dissociated in the supersonic expansion of the carrier (rare) gas to maximize the flux of $O(^1D_2)$ and
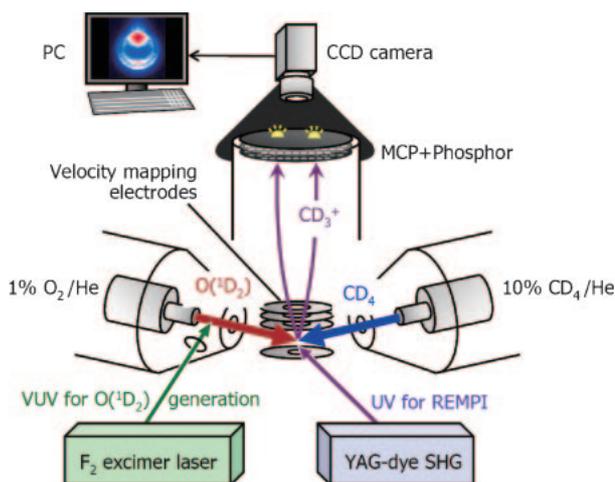

Fig. 2. Schematic illustration of crossed molecular beam ion imaging experiment for studying the $O(^1D_2) + CD_4 \rightarrow OD + CD_3$ reaction.

control their velocities; since the speed of $O(^1D_2)$ essentially becomes the same as that of the carrier gas, the collision energy between $O(^1D_2)$ and methane can be varied by changing the rare gas (He, Ne, Ar, or Kr) used as the carrier. The $O(^1D_2)$ atomic beam is crossed with a CD_4 molecular beam in a scattering chamber[33),34] and the CD_3 product is state-selectively ionized by resonance-enhanced multiphoton ionization via the $3p_z$ Rydberg state using a tunable nanosecond UV laser. (CD_4 is used because CD_3 radicals are less predissociative than CH_3 in the $3p_z$ Rydberg state. The CD_3^+ is also experimentally much less affected than CH_3^+ by background signals from hydrocarbon contaminants from sources such as pump oils.) The three-dimensional distribution of CD_3^+ ions is accelerated in an electric field and projected onto a two-dimensional position-sensitive detector.[33),34] The observed image is corrected for the apparatus function and numerically inverted to the speed and angular distributions of CD_3.

Figure 3 shows examples of the speed and angular distributions inverted from the observed images of the CD_3 product in the vibrational ground state.[33] Figures 3(a)–(c) correspond to the final rotational states of $J = 3$, 5 and 7, respectively. All these distributions exhibit strong forward scattering, in agreement with Fig. 1. The striking feature of the distributions in Fig. 3 is that the backward scattering component exhibits a discrete speed distribution. The kinetic energy of the state-selected CD_3 is related to the internal energy of OD by the following energy conservation relation:
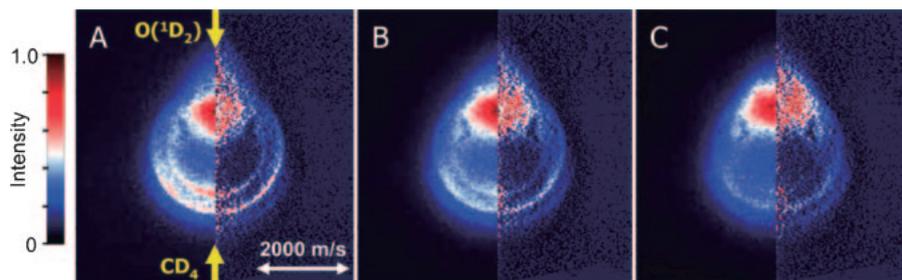
Fig. 3. False-color map of scattering distribution of the CD_3 product in the vibrational ground state. The rotational states of the products are (A) $J = 3$, (B) 5, and (C) 7. The left and right sides of each image respectively show the observed image and the two-dimensional slice of three-dimensional scattering distribution. The yellow arrows indicate the directions of the atomic and molecular beams. Forward scattering means ejection of a CD_3 radical in the direction of the CD_4 beam. Reproduced with permission from Ref. 33.

$$\Delta H + E_{\text{coll}} - E_{\text{rovib}}(CD_3) - E_{\text{trans}} = E_{\text{rovib}}(OD) \quad [1]$$

where ΔH is the exothermicity of the reaction, E_{coll} is the collision energy, $E_{\text{rovib}}(CD_3)$ is the rovibrational energy of CD_3, E_{trans} is the total translational energy of both products, and $E_{\text{rovib}}(OD)$ is the rovibrational energy of OD. The observed speed distributions of CD_3 reveal that the counterpart OD radicals are formed in the vibrationally excited states of $v = 4$–6. The strong vibrational excitation of OD is typical for an abstraction reaction with an early barrier. The discrete ring structure indicates that rotation of OD is only weakly excited. This weak rotational excitation is indicative of the collinear transition state that is expected for the abstraction pathway; the observed feature of backward scattering is rather similar to that of $F(^2P) + CD_4$.[35] The abstraction/insertion ratio diminishes for higher rotational states in Fig. 3 because the abstraction process has weaker rotational excitation than the insertion process. The forward scattering is structureless, even in our state-resolved measurements. This implies that the rotational excitation of the OD counterpart is quite strong in the insertion mechanism, in agreement with laser-induced fluorescence measurements of OH for $O(^1D) + CH_4$.[27]

    The angular distributions of CD_3 in the excited vibrational states of ν_2 (out-of-plane bending) mode (data not shown) exhibit essentially the same characteristics as the vibrational ground state. However, as shown in Fig. 4, the CD_3 products in the excited state of a symmetric C–D stretching vibration (v_1) do not exhibit a discrete speed distribution in the backward direction, indicating that CD_3 ($v_1 = 1$) is produced only in the insertion pathway; the excitation of C–D stretching is ascribed to vibrational coupling in the methanol intermediate.
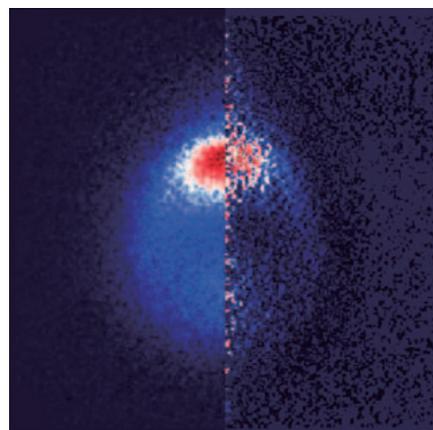

Fig. 4. Scattering distribution of the CD_3 ($v_1 = 1$) products. The Q-branch peak of the 1_1^1 vibronic band was employed in this measurement and the off-resonance image was subtracted. The left and right sides of each image respectively show the observed image and a two-dimensional slice of the three-dimensional scattering distribution. Comparison with Fig. 3 reveals that the backward scattering component is missing. Reproduced with permission from Ref. 33.

The strong forward scattering in Fig. 4 indicates that the CD_3OD complex has an extremely short lifetime. The vibrational distribution of CD_3 measured by the crossed-beam experiment is consistent with weak vibrational excitation of CH_3 observed by infrared diode laser spectroscopy.[26] We measured the rotational distribution of CD_3 produced by crossed-beam scattering and found that CD_3 radicals are created in low K states, where K is the quantum number of the angular momentum projected on the top axis of the CD_3 radical. Low K states correspond to tumbling rotation of CD_3.[33] Very recently, we performed a similar crossed-beam imaging experiment on $O(^1D_2) + CH_4 \rightarrow OH + CH_3$ and observed
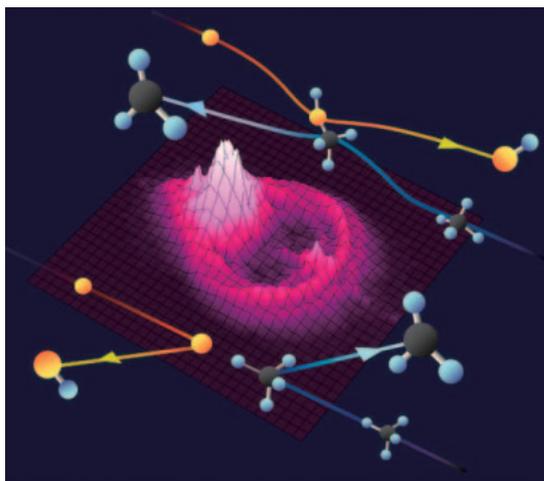
Fig. 5. Graphical presentation of the two reaction pathways. Insertion occurs with a large impact parameter and results in forward scattering of rotationally excited products. Abstraction reaction occurs via a collinear transition state and results in the backward scattering of weakly excited products.

essentially the same characteristics as $O(^1D_2) + CD_4 \rightarrow OD + CD_3$. Figure 5 shows a graphical depiction of the reaction mechanism of $O(^1D_2) + CH_4 \rightarrow OH + CH_3$.

Theoretical estimates of the reaction barrier height have ambiguities of ca. 2 kcal/mol. *Ab initio* calculations using CASPT2 and the basis set 6-311G(2df, 2pd) predict that the insertion pathway is barrierless, whereas the abstraction pathway has a barrier height of 1.2 kcal/mol.[36] Restricted internally contracted multireference configuration interaction calculations at the complete basis set limit predict that the insertion pathway will have a barrier height of 1.47 kcal/mol (without correcting for the zero-point energy).[37] Further experimental studies are currently being conducted in our laboratory to investigate the reaction barriers and the collision energy dependence of the dynamics. Accurate dynamical calculations of the *ab initio* potential energy surfaces are highly computationally demanding, yet they will be very useful for understanding the dynamics.

2. Ultrafast photoelectron imaging: real-time observation of nonadiabatic dynamics

Although sophisticated crossed-beam ion imaging experiments provide fine details of reaction dynamics, they observe only the products after a reaction occurs. Some important aspects of chemical reaction dynamics can be studied only by real-time observations. One example is the nonadiabatic dynamics of polyatomic molecules. The Born–Oppenheimer approximation facilitates a quantum-mechanical description of a chemical reaction[38] by enabling the equations of motions for electrons and nuclei to be separated. In the Born–Oppenheimer approximation, chemical reactions are viewed as classical trajectories or quantum-mechanical wave packet motions of the nuclear geometry on electronic potential energy surfaces. However, the Born–Oppenheimer approximation breaks down when different electronic states are close in energy; this gives rise to complex yet interesting nonadiabatic dynamics. Nonadiabatic transitions frequently occur in polyatomic molecules because they have several electronic states with similar energies and their multidimensional potential energy surfaces frequently undergo avoided crossings. It is thus important to identify nonadiabatic transitions in experimental and theoretical studies of polyatomic reactions.

Real-time observations of bimolecular reactions are not currently feasible because the timing of collisions cannot be controlled more accurately than the reaction time. Consequently, bimolecular dynamics is studied only from the asymptotic states of products using the crossed molecular beam scattering, as described in the previous section. On the other hand, ultrafast spectroscopy permits real-time observation of the nonadiabatic dynamics of photo-induced unimolecular reactions.

Pyrazine $(C_4H_4N_2)$ is one of the most fundamental heteroaromatic molecules.[39]–[49] Its broad $S_2(^1B_{2u}, \pi\pi^*)$–$S_0(^1A_g)$ photoabsorption spectrum suggests that the S_2 state undergoes ultrafast electronic deactivation (internal conversion) within 30 fs. This ultrafast deactivation originates from the conical intersection between the S_2 and $S_1(^1B_{3u}, n\pi^*)$ potential energy surfaces (see Fig. 6).[41] In a diatomic molecule, the von Neumann–Wigner noncrossing rule prohibits degeneracy of electronic states with the same symmetry so that their potential energy curves have avoided crossings.[50] For a nonlinear polyatomic molecule with N vibrational degrees of freedom, potential energy surfaces can be degenerate to form a seam of crossings in N–2 dimensional space (known as a conical intersection). The conical intersection is the most important topographical feature of multi-dimensional surfaces of polyatomic molecules.[51]–[55] Ultrafast internal conversion of pyrazine via conical intersection has been extensively investigated theoretically.[39]–[49]
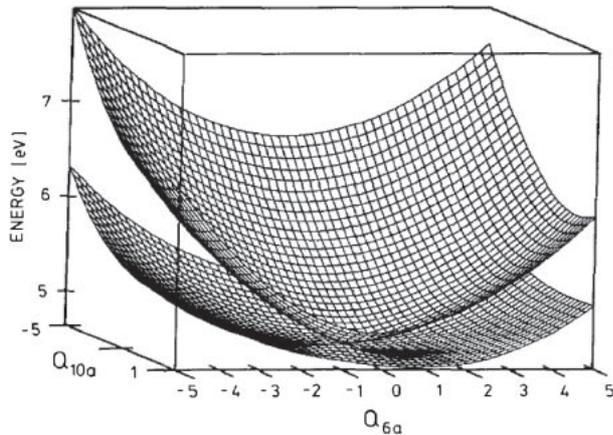
Fig. 6.   Conical intersection of S_2 and S_1 adiabatic potential energy surfaces of pyrazine in the two-dimensional space spanned by Q_{10a} and Q_{6a}. Reproduced with permission from Ref. 47.

Since a nonadiabatic transition abruptly alters the electronic character, it is most sensitively detected by measuring the electron distribution. However, the total electron density of a molecule is not the most suitable observable for this purpose because the total electron density distribution in a molecule does not change at the instant of a nonadiabatic transition. Photoelectron spectroscopy enables selective observation of valence electrons that play central roles in nonadiabatic transitions. The angular distribution of a photoelectron is a particularly important observable because a nonadiabatic transition changes the three-dimensional shape of an occupied electron orbital and affects the photoelectron wavefunction. Ultrafast photoelectron imaging visualizes the photoelectron speed and angular distributions as a movie with a femtosecond time resolution and enables identification of nonadiabatic transitions.[56)–58)]

How are the photoelectron kinetic energy and angular distributions expressed? In the absence of an external electromagnetic field, molecules in the gas phase have random alignment of the molecular axes. One-photon absorption induced by a linearly polarized pump pulse promotes molecules to an excited state whose transition dipole moments are favorably aligned with the electric field vector of the pump pulse. The probe pulse induces ejection of a photoelectron from this aligned ensemble of molecules in the excited state. Based on these two optical steps, the final photoelectron kinetic energy and angular distribution can be expressed by

$$I(E, \theta, t) = \frac{\sigma(E, t)}{4\pi} \{1 + \beta_2(E, t)P_2(\cos\theta)$$
$$+ \beta_4(E, t)P_4(\cos\theta)\} \qquad [2]$$

for a probe pulse whose linear polarization is parallel to that of the pump pulse. In this expression, E is the photoelectron kinetic energy, θ is the electron ejection angle relative to the laser polarization direction, and t is the pump–probe time delay. $P_n(x)$ is the nth-order Legendre polynomial. $\sigma(E, t)$ represents the photoelectron kinetic energy distribution (*i.e.*, the photoelectron spectrum). The anisotropy parameters, $\beta_2(E, t)$ and $\beta_4(E, t)$, contain information about the spatial distribution of an ionized orbital. Two-dimensional maps of $\sigma(E, t)$ and $\beta_2(E, t)$ against time and energy are the key observables for analyzing nonadiabatic dynamics.

Ultrafast photoelectron imaging combines the ultrafast pump–probe method and two-dimensional position-sensitive detection of electrons. An expanding distribution of photoelectrons is created when a laser pulse ionizes molecules in the vacuum chamber. Photoelectron imaging accelerates these electrons in a static electric field and projects them onto a two-dimensional position-sensitive detector (Fig. 7). Since this method enables the total speed and angular distributions of photoelectrons to be simultaneously measured on a shot-to-shot basis, it achieves unprecedentedly high efficiency and accuracy. Ultrashort UV pulses required for this experiment can be generated by nonlinear optical processes in rare gases. Since a gas has a small nonlinear susceptibility, a long interaction length between laser pulses and a gas medium is required to realize efficient wavelength conversion. To obtain a sufficiently long interaction length, we employ filamentation propagation of intense laser pulses; when an intense laser pulse propagates through a gas, it is self-focused by the optical Kerr effect and defocused by the plasma created by ionization of the gas. Consequently, a laser beam propagates through a gas while maintaining a small beam diameter for a length that is considerably greater than the confocal parameter.[59)] We introduce 775 and 388 nm pulses to Ne (0.08 MPa) and induce cascaded four-wave mixing of $2\hbar\omega_{388} - \hbar\omega_{775} \rightarrow \hbar\omega_{264}$ and $\hbar\omega_{264} + \hbar\omega_{388} - \hbar\omega_{775} \rightarrow \hbar\omega_{198}$ to generate 264 and 198 nm pulses (Fig. 7).[60)] These pulses are separated and compressed using a grating-based compressor to achieve pulse durations of 14 and 17 fs, respectively.[60),61)]

We excited pyrazine molecules in a supersonic molecular beam using the 264 nm pulse and sub-
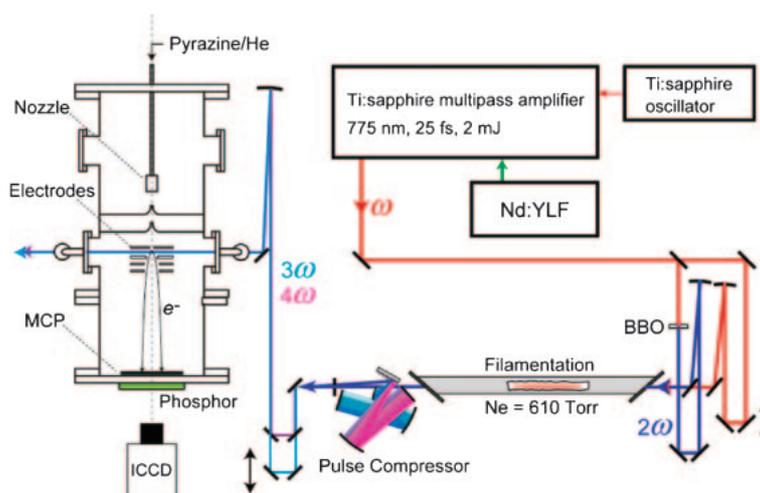
Fig. 7.   Schematic diagram of filamentation four-wave mixing to generate sub-20 fs deep UV pulses and our photoelectron imaging setup.

sequently ionized them with the 198 nm pulse. Figure 8b shows the photoelectron intensity observed as a function of the pump–probe time delay. The intensity decays rapidly in the first 100 fs and subsequently plateaus.[62),63)] This time profile is well explained by assuming rapid decay of optically excited S_2 (red) and formation of S_1 (blue) by internal conversion from S_2. In the negative delay time range, the 198 nm pulse excites pyrazine to S_3 and the 264 nm pulse ionizes (green); since this is unrelated to the present discussion, we neglect it here. The $S_2 \rightarrow S_1$ internal conversion time constants are determined as 23 ± 4 fs for pyrazine-h4 and 20 ± 2 fs for pyrazine-d4. Close examination reveals that the signal oscillates in the plateau region. The Fourier transform of this feature ($t > 50$ fs) exhibits a frequency component of 560 ± 40 cm^{-1} for pyrazine and 550 ± 40 cm^{-1} for pyrazine-d4. Based on these frequencies, the oscillation is assigned to vibrational wave packet motion of mode 6a in S_1 created by internal conversion.

We now examine the kinetic energy distribution of photoelectrons. Figure 8a shows a time–energy map of $\sigma(E, t)$. The colors yellow, red and violet indicate decreasing intensities. $\sigma(E, t)$ exhibits no marked change in distribution; the intensity diminishes gradually from a low to high kinetic energy at all times. The kinetic energy distribution does not change on internal conversion, because photoionization predominantly occurs as $D_0(n^{-1}) \leftarrow S_1(n, \pi^*)$ and $D_1(\pi^{-1}) \leftarrow S_2(\pi, \pi^*)$ (see Fig. 9) and these vertical ionization energies are almost identical.[64),65)] In other words, removal of a π^* electron always requires the same energy.

How is the photoelectron angular distribution? Figure 8c shows a time–energy map of $\beta_2(E, t)$; the positive (blue-green) and negative (red) values respectively indicate preferential ejection of an electron parallel and perpendicular to the probe laser polarization. The most distinctive feature in $\beta_2(E, t)$ is the sudden change at ca. 30 fs; this notable change in $\beta_2(E, t)$ is unambiguous evidence for $S_2 \rightarrow S_1$ internal conversion. (The influence of molecular rotation can be neglected on this time scale.) After 30 fs, $\beta_2(E, t)$ does not change, because the electronic character remains (n, π^*). The lack of restoration of the (π, π^*) character is related to the photoexcitation energy; in our experiment, photoexcitation of pyrazine near the S_2 origin prepares a wave packet with a small vibrational excess energy in S_2. Consequently, if the vibrational energy flows into various modes in S_1, the wave packet has no opportunity to return to the Franck–Condon region in S_2.

Ultrafast $S_2 \rightarrow S_1$ internal conversion of pyrazine has been considered as a two-state problem via a conical intersection. The above-described results of ultrafast photoelectron imaging are consistent with this well-accepted picture. On the other hand, recent quantum chemical calculations suggest that optically dark electronic states of ^1A_u and $^1B_{2g}$ are also involved in the ultrafast internal conversion dynamics of pyrazine and that a fraction of the population in S_2 flows into these states.[40),66)] The proposed mechanism is currently being investigated in our laboratory by ultrafast photoelectron imaging using a vacuum UV probe pulse (160 nm).
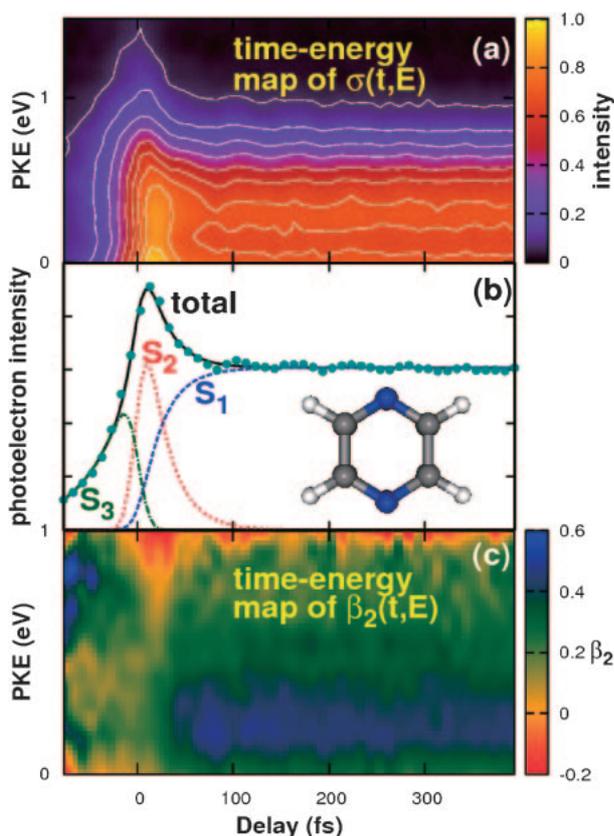
Fig. 8. (a) Time-evolution of photoelectron kinetic energy distribution, $\sigma(E, t)$. (b) Temporal profiles of total photoelectron signals in $(1 + 1')$ TRPEI of pyrazine-h4. The observed data are well explained by three components: single-exponential decay of S_2 (red); corresponding increase in S_1 (blue) in the positive time delay; and single-exponential decay of S_3 (green) in the negative-time delay. The fitting result is shown by the solid line. (c) Time evolution of photoelectron angular anisotropy parameter $\beta_2(E, t)$.

3. New challenge: ultrafast photoelectron spectroscopy of nonadiabatic dynamics in liquids

The preceding two sections discussed chemical dynamics in the gas phase. The study of gas-phase reactions provides the basis for understanding more complex dynamics in condensed phases. The greatest difference between gas and condensed phases is that solvent effects play important roles in the latter phases. Despite not fully understanding the mechanisms involved, chemists have utilized solvent effects for centuries to alter potential energy surfaces and reaction dynamics. It is thus exciting to apply ultrafast photoelectron spectroscopy to liquids to investigate static and dynamic solvent effects
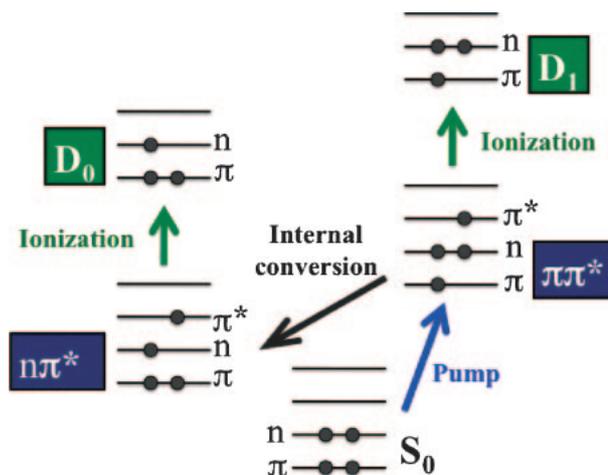

Fig. 9. Photoionization schemes of pyrazine within the framework of the frozen-core approximation.

and nonadiabatic processes, particularly in aqueous solutions.

Siegbahn[67] pioneered photoelectron spectroscopy of liquids in the 1970s. The technical problem to introduce volatile liquids into a photoelectron spectrometer was solved to a large extent by a liquid beam technique developed by Faubel and coworkers[68] in the 1980s. Winter and coworkers[69] performed photoelectron spectroscopy of liquid beams with third-generation synchrotron radiation. Kondow and Mafune combined a laser with liquid beams to perform photoionization mass spectrometry in 1992.[70] It took nearly two decades before ultrafast photoelectron spectroscopy of liquids was realized in 2010.[71)–73] This section describes this very new research field.

An electron passing through a liquid is scattered by solvent molecules. This scattering determines the escape depth of a photoelectron (and hence the probing depth of photoelectron spectroscopy). Therefore, the inelastic mean free path of an electron in the bulk is a very important quantity. However, the inelastic mean free path is not well understood for any liquid. It is thus necessary to speculate about it based on those in solids. Experimental studies of solid materials show that the mean free path becomes minimal ($<1\,\mathrm{nm}$) for kinetic energies in the range 50–$100\,\mathrm{eV}$.[74] Inelastic scattering of an electron in amorphous ice indicates that electron energy losses greater than $1\,\mathrm{eV}$ rarely occurs for kinetic energies smaller than the HOMO–LUMO gap ($\sim 7\,\mathrm{eV}$) of bulk water.[75] This is because such low-energy electrons cannot excite the valence electrons of water and
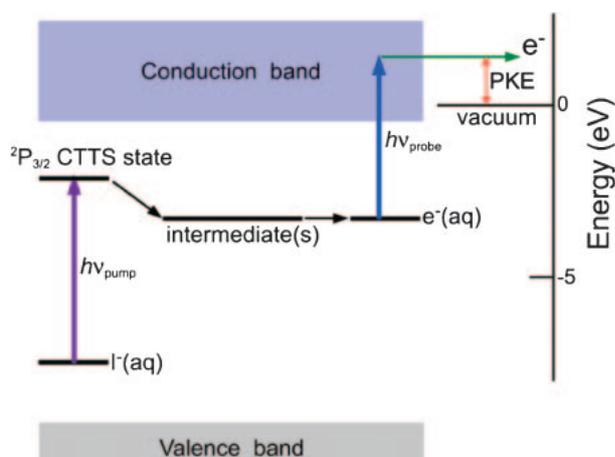
Fig. 10. Schematic energy diagram of time-resolved photoelectron spectroscopy of charge-transfer-to solvent reaction. Reproduced with permission from Ref. 94.
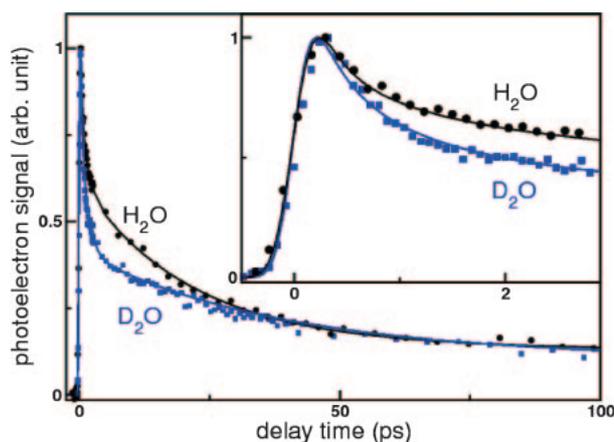

Fig. 11. Photoelectron signal intensity as a function of pump–probe time delay observed for charge-transfer-to-solvent reaction from I^- to bulk water: the sample solutions were $0.1\,M$ aqueous NaI solution in H_2O (black) and D_2O (blue). The schematic energy diagram of the experiment is shown in Fig. 10. The cross correlation of the pump and probe laser pulses was ca. $300\,fs$. A hemispherical electron energy analyzer was used to measure the photoelectron spectrum at each time delay and the spectrum was integrated over the photoelectron kinetic energy to obtain each data point. From Ref. 94.

hence interact only with phonons. Since electron–phonon scattering has a considerably smaller cross section than electron–electron scattering, the inelastic mean free path (and hence the probing depth of photoelectron spectroscopy) increases with decreasing kinetic energy. (Another extreme case is hard-X-ray photoelectron spectroscopy, which is also bulk sensitive.)

Using ultrafast photoelectron spectroscopy of liquids, we studied the charge-transfer-to-solvent (CTTS) reaction from I^-(aq) to bulk water (see Fig. 10).[76)–78)] A hydrated I^- atom has an electron binding energy of $8.0\,eV$ and its ground state lies in the band gap of bulk water; the electron binding energy of bulk water is $11.2\,eV$.[79)] The UV absorption maximum of I^-(aq) is at $225\,nm$, corresponding to excitation to the metastable (CTTS) electronic state. The CTTS state rapidly undergoes exothermic electron transfer to bulk water. When the excess electron migrates into bulk water, a local hydrogen-bonding network around the I atom and the excess electron change drastically due to reorientation of water molecules; I^- and an excess electron cloud are hydrophilic, whereas a neutral I atom is hydrophobic. Thus, the CTTS dynamics is strongly coupled with the solvation dynamics. The I atom has no internal degrees of freedom besides electronic motion, making it a suitable solute for investigating the CTTS dynamics. We excited I^-(aq) with the $226\,nm$ pump pulse and photodetached the excess electron with a time-delayed $260\,nm$ probe pulse. A hemispherical electron energy analyzer with extensive differential pumping was employed.[80)]

Figure 11 compares the photoelectron signal intensity, $I(t)$, observed for aqueous NaI solutions of H_2O and D_2O as a function of the pump–probe delay time. The figure indicates a clear isotope effect: the photoelectron intensity in the first few picoseconds diminishes much faster in D_2O than in H_2O, while the opposite is true in the subsequent $30\,ps$. Another isotope effect is seen in Fig. 12 that shows $\sigma(E, t)$ for solutions in H_2O and D_2O. $\sigma(E, t)$ has similar general features for H_2O and D_2O; however, the spectral width of $\sigma(E, t)$ is narrower and its intensity diminishes faster in D_2O than in H_2O. The time dependences of the photoelectron intensity and kinetic energy distribution can be explained by the mechanism illustrated in Fig. 13. After photoexcitation of I^- to a metastable state, the excess electron distribution becomes asymmetric in the hydration shell and separated from a neutral I atom. Calculations for Cl^- and water suggest that attractive interactions occur between a neutral atom and a hydrated electron;[81)] a similar attraction is anticipated between an I atom and a hydrated electron. The hydrated electron and I atom are finally separated by diffusion. The photon energy of our probe laser pulse is higher than the binding energies of the CTTS state, the contact pair state, the solvent separated state, and a free hydrated electron, but it is lower than the ground state of I^-(aq). Therefore, the
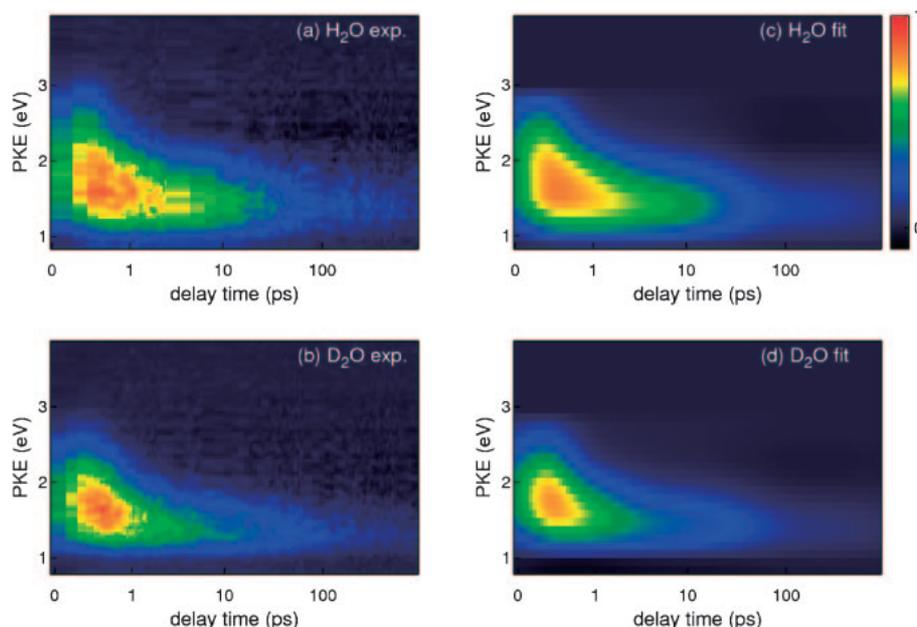
Fig. 12. Two-dimensional false-color map for photoelectron kinetic energy distributions measured for charge-transfer-to-solvent reaction from I^- to bulk water for various pump–probe time delays. The schematic energy diagram of the experiment is shown in Fig. 9. Experimental data for 0.1 M aqueous NaI solution in (a) H_2O and (b) D_2O. (c) and (d) show the results of global fitting of experimental data using a kinetic model. From Ref. 94.
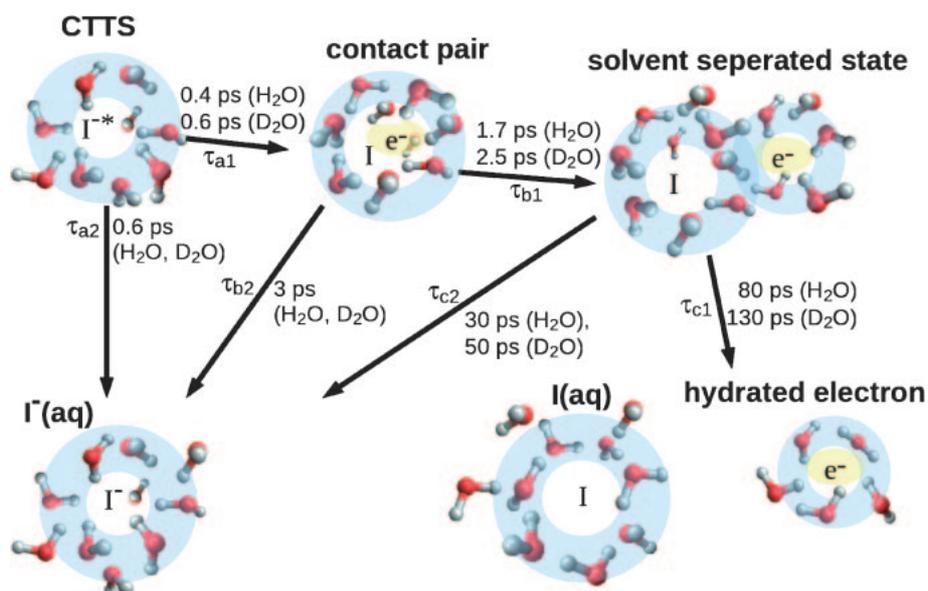

Fig. 13. Graphical presentation of our kinetic model with some representative time constants for the charge-transfer-to-solvent reaction from I^- to bulk water.

disappearance of the photoelectron signal in Fig. 11 is ascribed to internal conversion to the ground electronic state of I^-(aq); *i.e.*, geminate recombination of an electron and an I atom. In the initial steps

of the CTTS reaction, H_2O has a faster librational response than D_2O. Consequently, the quantum yield of internal conversion and the loss of electron signal are greater in D_2O during the early stages of the

reaction. On the other hand, internal conversion is nearly two times faster in H_2O than in D_2O during the later stages of the CTTS reaction.

The CTTS reaction for bulk water ultimately creates hydrated electrons,[56),71)–73),82)–94)] which are the most important transient species in radiation chemistry and biology. The electron binding energy of a hydrated electron has been speculated to be 3.3 eV, although no direct measurement has been performed. Our photoelectron spectroscopy of liquids has determined that the electron binding energy of a hydrated electron is 3.4 eV and that the energies of solvated electrons in methanol and ethanol are 3.5 and 3.3 eV, respectively.[66),72),73),94),95)] Interestingly, the electron binding energy of a hydrated electron agrees with a previous estimate (3.3 eV) obtained by extrapolating the binding energies in negatively charged water clusters.[84)] On the other hand, the electron binding energy of a solvated electron in methanol is much greater than the estimate (2.6 eV) from corresponding cluster values.[96)] The cause of this interesting difference is currently being investigated.

Ultrafast photoelectron spectroscopy of liquids is a very young field and there are many unsolved problems for this methodology. On the other hand, it is promising for elucidating electronic dynamics in solution and providing important new knowledge for chemistry, physics and biology.

Acknowledgments

References

1)   Taylor, E.H. and Datz, S. (1955) Study of chemical reaction mechanisms with molecular beams—the Reaction of K with HBr. J. Chem. Phys. **23**, 1711–1718.
2)   Lee, Y.T., McDonald, J.D., LeBreton, P.R. and Herschbach, D.R. (1969) Molecular beam reactive scattering apparatus with electron bombardment detector. Rev. Sci. Instrum. **40**, 1402–1408.
3)   Kinsey, J.L. (1977) Fourier-transform doppler spectroscopy—New means of obtaining velocity-angle distributions in scattering experiments. J. Chem. Phys. **66**, 2560–2565.
4)   Murphy, E.J., Brophy, J.H., Arnold, G.S., Dimpfl, W.L. and Kinsey, J.L. (1979) Velocity and angular-distributions of reactive collisions from Fourier-transform Doppler spectroscopy—1st experimental results. J. Chem. Phys. **70**, 5910–5911.
5)   Buntine, M.A., Baldwin, D.P., Zare, R.N. and

Chandler, D.W. (1991) Application of ion imaging to the atom-molecule exchange-reaction—H+HI→H_2+I. J. Chem. Phys. **94**, 4672–4675.
6)   Girard, B., Billy, N., Gouédard, G. and Vigué, J. (1991) Differential cross-section as a function of the product internal state—the F+I_2→IF(v,J)+I reactive collision. J. Chem. Phys. **95**, 4056–4069.
7)   Suits, A.G., Bontuyan, L.S., Houston, P.L. and Whitaker, B.J. (1992) Differential cross-sections for state-selected products by direct imaging—Ar+NO. J. Chem. Phys. **96**, 8618–8620.
8)   Schnieder, L., Seekamprahn, K., Borkowski, J., Wrede, E., Welge, K.H., Aoiz, F.J., Banares, L., Dmello, M.J., Herrero, V.J., Rabanos, V.S. and Wyatt, R.E. (1995) Experimental studies and theoretical predictions for the H+D_2→HD+D reaction. Science **269**, 207–210.
9)   Chandler, D.W. and Houston, P.L. (1987) Two-dimensional imaging of state-selected photodissociation products detected by multiphoton ionization. J. Chem. Phys. **87**, 1445–1447.
10) Eppink, A.T.J.B. and Parker, D.H. (1997) Velocity map imaging of ions and electrons using electrostatic lenses: Application in photoelectron and photofragment ion imaging of molecular oxygen. Rev. Sci. Instrum. **68**, 3477–3484.
11) Continetti, R.E., Balko, B.A. and Lee, Y.T. (1990) Crossed molecular-beams study of the reaction D+H_2→DH+H at collision energies of 0.53 and 1.01 eV. J. Chem. Phys. **93**, 5719–5740.
12) Wrede, E., Schnieder, L., Welge, K.H., Aoiz, F.J., Banares, L., Herrero, V.J., MartinezHaya, B. and Rabanos, V.S. (1997) The H+D_2 reaction in the vicinity of the conical intersection. J. Chem. Phys. **106**, 7862–7864.
13) Schnieder, L., SeekampRahn, K., Wrede, E. and Welge, K.H. (1997) Experimental determination of quantum state resolved differential cross sections for the hydrogen exchange reaction H+D_2→HD+D. J. Chem. Phys. **107**, 6175–6195.
14) Neumark, D.M., Wodtke, A.M., Robinson, G.N., Hayden, C.C. and Lee, Y.T. (1985) Molecular-beam studies of the F+H_2 reaction. J. Chem. Phys. **82**, 3045–3066.
15) Neumark, D.M., Wodtke, A.M., Robinson, G.N., Hayden, C.C., Shobatake, K., Sparks, R.K., Schafer, T.P. and Lee, Y.T. (1985) Molecular-beam studies of the F+D_2 and F+HD reactions. J. Chem. Phys. **82**, 3067–3077.
16) Skodje, R.T., Skouteris, D., Manolopoulos, D.E., Lee, S.H., Dong, F. and Liu, K.P. (2000) Resonance-mediated chemical reaction: F+HD→HF+D. Phys. Rev. Lett. **85**, 1206–1209.
17) Qiu, M.H., Ren, Z.F., Che, L., Dai, D.X., Harich, S.A., Wang, X.Y., Yang, X.M., Xu, C.X., Xie, D.Q., Gustafsson, M., Skodje, R.T., Sun, Z.G. and Zhang, D.H. (2006) Observation of Feshbach resonances in the F+H_2→HF+H reaction. Science **311**, 1440–1443.
18) Che, L., Ren, Z.F., Wang, X.G., Dong, W.R., Dai, D.X., Wang, X.Y., Zhang, D.H., Yang, X.M., Sheng, L.S., Li, G.L., Werner, H.J., Lique, F. and

Alexander, M.H. (2007) Breakdown of the Born-Oppenheimer approximation in the F+o-D$_2$→DF+D reaction. Science **317**, 1061–1064.

19) Hsu, Y.T., Wang, J.H. and Liu, K.P. (1997) Reaction dynamics of O(^1D)+H$_2$, D$_2$, and HD: Direct evidence for the elusive abstraction pathway and the estimation of its branching. J. Chem. Phys. **107**, 2351–2356.

20) Hsu, Y.T. and Liu, K.P. (1997) Product state(s)-resolved differential cross section of the reaction O(^1D)+HD→OH(v,j)+D. J. Chem. Phys. **107**, 1664–1667.

21) Liu, X.H., Lin, J.J., Harich, S., Schatz, G.C. and Yang, X.M. (2000) A quantum state-resolved insertion reaction: O(^1D)+H$_2$(J=0)→OH($^2\Pi$, v, N)+H(^{2}S). Science **289**, 1536–1538.

22) Liu, X.H., Lin, J.J., Harich, S.A. and Yang, X.M. (2001) State-to-state dynamics for $O(^1D)$+D$_2$ → OD+D: Evidence for a collinear abstraction mechanism. Phys. Rev. Lett. **86**, 408–411.

23) Lin, J.J., Shu, J., Lee, Y.T. and Yang, X. (2000) Multiple dynamical pathways in the O(^1D)+CH$_4$ reaction: A comprehensive crossed beam study. J. Chem. Phys. **113**, 5287–5301.

24) Paraskevopoulos, G. and Cvetanovic, R.J. (1969) Competitive reactions of excited oxygen atoms, O(^1D). J. Am. Chem. Soc. **91**, 7572–7577.

25) Lin, C.L. and Demore, W.B. (1973) Reactions of O(^1D) with methane and ethane. J. Phys. Chem. **77**, 863–869.

26) Suzuki, T. and Hirota, E. (1993) Vibrational distribution of CH$_3$ produced by the reaction of O($^1D_2$) atom with CH$_4$. J. Chem. Phys. **98**, 2387–2398.

27) Park, C.R. and Wiesenfeld, J.R. (1991) Full characterization of OH product energetics in the reaction of O($^1D_2$) with hydrocarbons. J. Chem. Phys. **95**, 8166–8177.

28) Miller, W.B., Safron, S.A. and Herschbach, D.R. (1967) Exchange reactions of alkali atoms with alkali halides—A collision complex mechanism. Discuss. Faraday Soc. **44**, 108–122.

29) Yonekura, N., Gebauer, C., Kohguchi, H. and Suzuki, T. (1999) A crossed molecular beam apparatus using high-resolution ion imaging. Rev. Sci. Instrum. **70**, 3265–3270.

30) Kohguchi, H., Suzuki, T. and Alexander, M.H. (2001) Fully state-resolved differential cross sections for the inelastic scattering of the open-shell NO molecule by Ar. Science **294**, 832–834.

31) Kohguchi, H., Suzuki, T., Nanbu, S., Ishida, T., Mil'nikov, G.V., Oloyede, P. and Nakamura, H. (2008) Collision energy dependence of the O(^1D)+HCl→OH+Cl(^{2}P) reaction studied by crossed beam scattering and quasiclassical trajectory calculations on ab initio potential energy surfaces. J. Phys. Chem. A **112**, 818–825.

32) Kohguchi, H. and Suzuki, T. (2006) A crossed molecular beam imaging study of the O($^1D_2$)+HCl→OH+Cl(^{2}P$_{J=3/2,1/2}$) reaction. ChemPhysChem **7**, 1250–1257.

33) Kohguchi, H., Ogi, Y. and Suzuki, T. (2011) Rovibrational state specific scattering distributions of the O(^1D)+CD$_4$→OD+CD$_3$ (v$_1$, v$_2$, N) reaction. Phys. Chem. Chem. Phys. **13**, 8371–8378.

34) Kohguchi, H., Ogi, Y. and Suzuki, T. (2008) Reaction mechanism duality in O($^1D_2$)+CD$_4$→OD+CD$_3$ identified from scattering distributions of rotationally state selected CD$_3$. Phys. Chem. Chem. Phys. **10**, 7222–7225.

35) Lin, J.J., Zhou, J.G., Shiu, W.C. and Liu, K.P. (2003) State-specific correlation of coincident product pairs in the F+CD$_4$ reaction. Science **300**, 966–969.

36) Hernando, J., Millan, J., Sayos, R. and Gonzalez, M. (2003) *Ab initio* study of the O(^1D)+CH$_4$(X^1A_1)→OH($X^2\Pi$)+CH$_3$(X^2A_2'') reaction: ground and excited potential energy surfaces. J. Chem. Phys. **119**, 9504–9512.

37) Yu, H.-G. and Muckerman, J.T. (2004) MRCI calculations of the lowest potential energy surface for CH$_3$OH and direct ab initio dynamics simulations of the O(^1D) + CH$_4$ reaction. J. Phys. Chem. A **108**, 8615–8623.

38) Born, M. and Oppenheimer, R. (1927) Quantum theory of molecules. Ann. Phys. **84**, 0457–0484.

39) Werner, U., Mitric, R. and Bonacic-Koutecky, V. (2010) Simulation of time resolved photoelectron spectra with Stieltjes imaging illustrated on ultrafast internal conversion in pyrazine. J. Chem. Phys. **132**, 174301.

40) Werner, U., Mitric, R., Suzuki, T. and Bonacic-Koutecky, V. (2008) Nonadiabatic dynamics within the time dependent density functional theory: Ultrafast photodynamics in pyrazine. Chem. Phys. **349**, 319–324.

41) Schneider, R. and Domcke, W. (1988) S$_1$-S$_2$ conical intersection and ultrafast S$_2$→S$_1$ internal-conversion in pyrazine. Chem. Phys. Lett. **150**, 235–242.

42) Seel, M. and Domcke, W. (1991) Femtosecond time-resolved ionization spectroscopy of ultrafast internal-conversion dynamics in polyatomic-molecules—Theory and computational studies. J. Chem. Phys. **95**, 7806–7822.

43) Seidner, L., Stock, G., Sobolewski, A.L. and Domcke, W. (1992) *Ab initio* characterization of the S$_1$-S$_2$ conical intersection in pyrazine and calculation of spectra. J. Chem. Phys. **96**, 5298–5309.

44) Sobolewski, A.L., Woywod, C. and Domcke, W. (1993) *Ab initio* investigation of potential-energy surfaces involved in the photophysics of benzene and pyrazine. J. Chem. Phys. **98**, 5627–5641.

45) Stock, G. and Domcke, W. (1993) Femtosecond spectroscopy of ultrafast nonadiabatic excited-state dynamics on the basis of ab initio potential-energy surfaces—the S$_2$ state of pyrazine. J. Phys. Chem. **97**, 12466–12472.

46) Stock, G., Woywod, C., Domcke, W., Swinney, T. and Hudson, B.S. (1995) Resonance raman-spectroscopy of the S$_1$ and S$_2$ states of pyrazine—experiment and first principles calculation of spectra. J. Chem. Phys. **103**, 6851–6860.

47) Woywod, C., Domcke, W., Sobolewski, A.L. and Werner, H.J. (1994) Characterization of the S$_1$-S$_2$

conical intersection in pyrazine using *ab initio* multiconfiguration self-consistent-field and multi-reference configuration-interaction methods. J. Chem. Phys. **100**, 1400–1413.

48) Raab, A., Worth, G.A., Meyer, H.D. and Cederbaum, L.S. (1999) Molecular dynamics of pyrazine after excitation to the S_2 electronic state using a realistic 24-mode model Hamiltonian. J. Chem. Phys. **110**, 936–946.

49) Worth, G.A., Meyer, H.D. and Cederbaum, L.S. (1996) The effect of a model environment on the S_2 absorption spectrum of pyrazine: A wave packet study treating all 24 vibrational modes. J. Chem. Phys. **105**, 4412–4426.

50) von Neumann, J. and Wigner, E. (1929) Concerning the behaviour of eigenvalues in adiabatic processes. Phys. Z. **30**, 467–470.

51) Bernardi, F., Olivucci, M. and Robb, M.A. (1996) Potential energy surface crossings in organic photochemistry. Chem. Soc. Rev. **25**, 321–328.

52) Domcke, W., Yarkony, D.R. and Koppel, H. (2011) Conical Intersections: Theory, Computation and Experiment, Vol. 17, World Scientific Publishing Co. Pte. Ltd., Singapore.

53) Domcke, W., Yarkony, D.R. and Koppel, H. (2004) Conical Intersections: Electronic Structure, Dynamics & Spectroscopy, Vol. 15, World Scientific Publishing Co. Pte. Ltd., Singapore.

54) Yarkony, D.R. (1998) Conical intersections: Diabolical and often misunderstood. Acc. Chem. Res. **31**, 511–518.

55) Yarkony, D.R. (1996) Diabolical conical intersections. Rev. Mod. Phys. **68**, 985–1013.

56) Suzuki, T. and Whitaker, B.J. (2001) Non-adiabatic effects in chemistry revealed by time-resolved charged-particle imaging. Int. Rev. Phys. Chem. **20**, 313–356.

57) Suzuki, T. (2006) Femtosecond time-resolved photoelectron imaging. Annu. Rev. Phys. Chem. **57**, 555–592.

58) Suzuki, T. (2012) Time-resolved photoelectron spectroscopy of non-adiabatic electronic dynamics in gas and liquid phases. Int. Rev. Phys. Chem. **31**, 265–318.

59) Chin, S.L. (2010), Femtosecond Laser Filamentation. Springer, New York.

60) Fuji, T., Horio, T. and Suzuki, T. (2007) Generation of 12 fs deep-ultraviolet pulses by four-wave mixing through filamentation in neon gas. Opt. Lett. **32**, 2481–2483.

61) Fuji, T., Suzuki, T., Serebryannikov, E.E. and Zheltikov, A. (2009) Experimental and theoretical investigation of a multicolor filament. Phys. Rev. A **80**, 063822.

62) Wang, L., Kohguchi, H. and Suzuki, T. (1999) Femtosecond time-resolved photoelectron imaging. Faraday Discuss. **113**, 37–46.

63) Stert, V., Farmanara, P. and Radloff, W. (2000) Electron configuration changes in excited pyrazine molecules analyzed by femtosecond time-resolved photoelectron spectroscopy. J. Chem. Phys. **112**, 4460–4464.

64) Oku, M., Hou, Y., Xing, X., Reed, B., Xu, H., Chang, C., Ng, C.-Y., Nishizawa, K., Ohshimo, K. and Suzuki, T. (2008) 3s Rydberg and cationic states of pyrazine studied by photoelectron spectroscopy. J. Phys. Chem. A **112**, 2293–2310.

65) Innes, K.K., Ross, I.G. and Moomaw, W.R. (1988) Electronic states of azabenzenes and azanaphthalenes—A revised and extended critical-review. J. Mol. Spectrosc. **132**, 492–544.

66) Lin, C.K., Niu, Y.L., Zhu, C.Y., Shuai, Z.G. and Lin, S.H. (2011) The role of the $n\pi^*$ ^1A_u state in the photoabsorption and relaxation of pyrazine. Chem. Asian J. **6**, 2977–2985.

67) Siegbahn, H. (1985) Electron-spectroscopy for chemical-analysis of liquids and solutions. J. Phys. Chem. **89**, 897–909.

68) Faubel, M., Steiner, B. and Toennies, J.P. (1997) Photoelectron spectroscopy of liquid water, some alcohols, and pure nonane in free micro jets. J. Chem. Phys. **106**, 9013–9031.

69) Winter, B. and Faubel, M. (2006) Photoemission from liquid aqueous solutions. Chem. Rev. **106**, 1176–1211.

70) Mafune, F., Takeda, Y., Nagata, T. and Kondow, T. (1992) Formation and ejection of cluster ions from a liquid beam of aniline—ethanol solution by laser photoionization. Chem. Phys. Lett. **199**, 615–620.

71) Tang, Y., Shen, H., Sekiguchi, K., Kurahashi, N., Mizuno, T., Suzuki, Y.I. and Suzuki, T. (2010) Direct measurement of vertical binding energy of a hydrated electron. Phys. Chem. Chem. Phys. **12**, 3653–3655.

72) Siefermann, K.R., Liu, Y.X., Lugovoy, E., Link, O., Faubel, M., Buck, U., Winter, B. and Abel, B. (2010) Binding energies, lifetimes and implications of bulk and interface solvated electrons in water. Nat. Chem. **2**, 274–279.

73) Lubcke, A., Buchner, F., Heine, N., Hertel, I.V. and Schultz, T. (2010) Time-resolved photoelectron spectroscopy of solvated electrons in aqueous NaI solution. Phys. Chem. Chem. Phys. **12**, 14629–14634.

74) Seah, M.P. and Dench, W.A. (1979) Quantitative electron spectroscopy of surfaces; a standard data base for electron inelastic mean free paths in solids. Surf. Interface Anal. **1**, 2–11.

75) Michaud, M., Wen, A. and Sanche, L. (2003) Cross sections for low-energy (1–100 eV) electron elastic and inelastic scattering in amorphous ice. Radiat. Res. **159**, 3–22.

76) Iglev, H., Trifonov, A., Thaller, A., Buchvarov, I., Fiebig, T. and Laubereau, A. (2005) Photoionization dynamics of an aqueous iodide solution: the temperature dependence. Chem. Phys. Lett. **403**, 198–204.

77) Kloepfer, J.A., Vilchiz, V.H., Lenchenkov, V.A., Germaine, A.C. and Bradforth, S.E. (2000) The ejection distribution of solvated electrons generated by the one-photon photodetachment of aqueous I- and two-photon ionization of the solvent. J. Chem. Phys. **113**, 6288–6307.

78) Chen, X.Y. and Bradforth, S.E. (2008) The ultrafast

dynamics of photodetachment. Annu. Rev. Phys. Chem. **59**, 203–231.

79) Winter, B., Weber, R., Hertel, I.V., Faubel, M., Jungwirth, P., Brown, E.C. and Bradforth, S.E. (2005) Electron binding energies of aqueous alkali and halide ions: EUV photoelectron spectroscopy of liquid solutions and combined ab initio and molecular dynamics calculations. J. Am. Chem. Soc. **127**, 7203–7214.

80) Nishizawa, K., Kurahashi, N., Sekiguchi, K., Mizuno, T., Ogi, Y., Horio, T., Oura, M., Kosugi, N. and Suzuki, T. (2011) High-resolution soft X-ray photoelectron spectroscopy of liquid water. Phys. Chem. Chem. Phys. **13**, 413–417.

81) Staib, A. and Borgis, D. (1996) Reaction pathways in the photodetachment of an electron from aqueous chloride: A quantum molecular dynamics study. J. Chem. Phys. **104**, 9027–9039.

82) Hart, E.J. and Boag, J.W. (1962) Absorption spectrum of hydrated electron in water and in aqueous solutions. J. Am. Chem. Soc. **84**, 4090–4095.

83) Bragg, A.E., Verlet, J.R.R., Kammrath, A., Cheshnovsky, O. and Neumark, D.M. (2004) Hydrated electron dynamics: From clusters to bulk. Science **306**, 669–671.

84) Coe, J.V., Lee, G.H., Eaton, J.G., Arnold, S.T., Sarkas, H.W., Bowen, K.H., Ludewigt, C., Haberland, H. and Worsnop, D.R. (1990) Photo-electron-spectroscopy of hydrated electron cluster anions, $(H_2O)^-_{n=2-69}$. J. Chem. Phys. **92**, 3980–3982.

85) Coe, J.V., Earhart, A.D., Cohen, M.H., Hoffman, G.J., Sarkas, H.W. and Bowen, K.H. (1997) Using cluster studies to approach the electronic structure of bulk water: Reassessing the vacuum level, conduction band edge, and band gap of water. J. Chem. Phys. **107**, 6023–6031.

86) Coe, J.V., Williams, S.M. and Bowen, K.H. (2008) Photoelectron spectra of hydrated electron clusters vs. cluster size: connecting to bulk. Int. Rev. Phys. Chem. **27**, 27–51.

87) Turi, L., Sheu, W.S. and Rossky, P.J. (2005) Characterization of excess electrons in water-cluster anions by quantum simulations. Science **309**, 914–917.

88) Turi, L., Sheu, W.S. and Rossky, P.J. (2005) Response to comment on "Characterization of excess electrons in water-cluster anions by quantum simulations". Science **310**, 1769.

89) Shkrob, I.A. (2007) The structure of the hydrated electron. Part 1. Magnetic resonance of internally trapping water anions: A density functional theory study. J. Phys. Chem. A **111**, 5223–5231.

90) Shkrob, I.A., Glover, W.J., Larsen, R.E. and Schwartz, B.J. (2007) The structure of the hydrated electron. Part 2. A mixed quantum/classical molecular dynamics embedded cluster density functional theory: Single-excitation configuration interaction study. J. Phys. Chem. A **111**, 5232–5243.

91) Larsen, R.E., Glover, W.J. and Schwartz, B.J. (2010) Does the hydrated electron occupy a cavity? Science **329**, 65–69.

92) Jacobson, L.D. and Herbert, J.M. (2011) Theoretical characterization of four distinct isomer types in hydrated-electron clusters, and proposed assignments for photoelectron spectra of water cluster anions. J. Am. Chem. Soc. **133**, 19889–19899.

93) Herbert, J.M. and Jacobson, L.D. (2011) Nature's most squishy ion: The important role of solvent polarization in the description of the hydrated electron. Int. Rev. Phys. Chem. **30**, 1–48.

94) Shreve, A.T., Yen, T.A. and Neumark, D.M. (2010) Photoelectron spectroscopy of hydrated electrons. Chem. Phys. Lett. **493**, 216–219.

95) Horio, T., Shen, H., Adachi, S. and Suzuki, T. (2012) Photoelectron spectra of solvated electrons in bulk water, methanol, and ethanol. Chem. Phys. Lett. **535**, 12–16.

96) Kammrath, A., Verlet, J.R.R., Griffin, G.B. and Neumark, D.M. (2006) Photoelectron imaging of large anionic methanol clusters: $(MeOH)^-_n$ ($n \sim 70$–460). J. Chem. Phys. **125**, 171102.

Profile

Toshinori Suzuki was born in 1961. As a freshman in Tohoku University he was inspired by quantum chemistry lectures given by the late Prof. Yoshito Amako, and he decided to study physical chemistry. He graduated from the university in 1984, and received the doctoral degree from the same university in 1988 under the supervision of Prof. Mitsuo Ito. He immediately joined the research group of Prof. Eizi Hirota at the Institute for Molecular Science as a technical associate and later became a research associate. During this period, he investigated $O(^1D)$ reaction with methane by infrared diode laser spectroscopy, and he decided to develop a crossed-beam ion imaging experiment for studying polyatomic reactions. In order to realize it, he resigned Institute for Molecular Science and joined Cornell University (Prof. Paul Houston) and the University of California, Berkeley (Prof. Yuan T. Lee) as a JSPS fellow for oversea studies. In 1992, he was appointed again by the Institute for Molecular Science as an associate professor and returned to Japan to start his research group. He initiated a crossed-beam imaging experiment and also realized femtosecond photoelectron imaging. In 2001, He moved to RIKEN to be a chief scientist and extended his research further. The crossed-beam imaging experiment on $O(^1D)$ reaction with methane was realized finally in 2008, 20 years after his first planning. He started the research project on chemical reaction dynamics in water using the advanced facilities of SPring-8 and SACLA (x-ray free electron laser), which is on going. In 2009, he became a professor of physical chemistry at Kyoto University to inspire, and be inspired by, young students. He received Broida Award, IBM Science Award, JSPS Prize and Commendation for Science and Technology by MEXT. He served as a president of Japan Society for Molecular Science for 2010–2012.